arXiv:1407.8381v2 [physics.flu-dyn] 1 Aug 2014

Non-isentropic layers in matter behind shock and ramp compression waves

K. V. Khishchenko[1] and A. E. Mayer[2]

[1] *Joint Institute for High Temperatures RAS, Izhorskaya 13 Bldg 2, Moscow 125412, Russia*

[2] *Chelyabinsk State University, Bratyev Kashirinykh 129, Chelyabinsk 454001, Russia*

(Dated: August 4, 2014)

Abstract

According to the ideal fluid dynamics approach, the temperature and entropy values of a medium undergo a jump increase in the shock front as well as on contact interface between different materials after the shock wave propagation, but remain constant behind the shock front out of the contact interface. In the real condensed matter, the shock fronts and transition regions near the interfaces have finite thicknesses; therefore, the temperature field is disturbed around the interfaces. In this work, such disturbances are numerically analyzed for the problems of formation of the steady shock wave at impact and ramp loading of metals, reflection of the steady shock wave from a free surface, and the shock wave passing through the interface between two different materials. Theoretical analysis and computations show that the non-isentropic layers (the high-entropy ones with the increased temperature and the low-entropy ones with the decreased temperature) arise near the interfaces in the above problems of shock and ramp loading. The impact produces the high-entropy layer; while the ramp loading can result in the both high- and low-entropy layers. At the shock wave passing through the interface, the high-entropy layer is formed in the lower-impedance material and the low-entropy—in the higher-impedance one. These high- and low-entropy layers should be taken into account in simulations of shock-wave processes in thin targets or in other cases where surface effects are important. For example, melting can take place in the high-entropy layer on the interface between colliding plates at shock intensities lower than the bulk melting threshold; also the temperature perturbations near the studied surface can affect the result of pyrometric measurements. To get high accuracy of simulations, one should exclude the artificial viscosity or its analogs from the numerical scheme and use the physically based dissipative processes (the physical viscosity, the plasticity, and the heat conductivity) for stabilization of the solution instead. Such a mathematical model with accounting for the dislocation plasticity is described here as well as the appropriate numerical scheme is proposed.

PACS numbers:

I. INTRODUCTION

Dynamic loading of thin metallic foils is under increasing attention[1–9] because it is the way to investigate the matter properties at extremely high strain rates. Plate impact is used for foils perhaps no thinner than 20 μm,[1–3] while the ultra-short intensive laser irradiation[4–9] can be used for foils of several microns in thickness or even thinner; the strain rate exceeds 10^9 s^{-1} in the latter case. Dynamic shear strength and spall strength tend to the theoretical limits at such extreme loading conditions;[4,7,10] these strengths are determined by inertness of development of the defects subsystems—dislocations and voids correspondingly.[10–12]

Compression waves formed under the laser irradiation in thin foils are treated as ramp waves[5,6] with a gradual increase of pressure. Such a wave should eventually breaks to the shock wave during its propagation into the bulk of target,[8,13,14] but it does not happen if the target is thin enough. The ramp waves can be created by other means as well, for example, using the magnetic pressure.[15,16] If the target is relatively thick and the pressure rise time is high, then the ramp-wave loading becomes nearly isentropic compression of substance because there is no discontinuity inherent to shock waves.[15] Shortening of the pressure rise time increases the entropy production in the ramp wave[16–18] and makes compression closer to that in a shock wave of the same intensity.

On the other hand, the shock wave is a discontinuity in analytical solution only for an ideal medium in absence of any dissipation. Shock waves in solids always have a finite rise time,[19–21] that means a finite thickness of the wave front, which is determined by the dissipative processes, plasticity first of all.[19] The differences from the ramp wave are as follows: (i) the unique dependence of the entropy jump upon the pressure or velocity jump, which is determined by the Hugoniot relation;[22] (ii) uncontrolled form of the shock front, which is often supposed to be a steady one.[20] The front thickness and strain rate of the steady shock wave are determined by the entropy jump and dissipative properties of the material—viscosity in fluids and plasticity in solids.[19,20,23]

An unsteady compression precedes the shock wave formation at both the plate impact and ramp loading. From the mechanical point of view, the plate impact is a kind of problem of the initial discontinuity break, rather the discontinuity of velocity field. Therefore, an initial strain rate (velocity gradient) is mathematically infinite, while physically restricted by the atom size (like in the molecular dynamics simulations of the impact[24,25]) or roughness

and inclination of the colliding metal surfaces. In any case, the initial strain rate at collision should be much higher than the strain rate at the steady shock. Thus, the shock wave formation at plate impact consists in gradual increase of the compression wave thickness and decrease of the corresponding strain rate with its motion inside the material. Similar to the ramp waves,[17,18] the strain rate decrease should be accompanied by the decrease of the entropy production and temperature rise behind the compression wave. Far from the impact surface the entropy increment tends to the jump determined by the Hugoniot relation. Near the impact surface the entropy increment should be higher and a high-entropy layer should be formed here. Formation of the shock wave at ramp loading is an opposite process with the gradual decrease of the compression wave thickness down to the shock front thickness; therefore a low-entropy layer should be formed in this case near the loaded surface.

The transition regions and corresponding high- and low-entropy layers can be negligibly small in comparison with the target thickness in the case of thick target. Meanwhile, those are essential for thin foils, such as used in experiments.[1–9] Therefore, formation of the non-isentropic layers should be investigated for adequate analysis of the experimental results. Moreover, the shock wave in solids may have an elastic precursor,[1,2,4–6,8,10,12] which decays with the distance,[19,21] that makes the shock wave unsteady in general. This feature probably can extend the non-isentropic layers in depth.

In this paper, the high- and low-entropy layers in metals near the loaded surface are studied numerically on the basis of the dislocation plasticity model.[12,26] The considered surface layers are qualitatively similar to the so called heating errors (or entropy traces, as in Russian terminology) produced by an artificial viscosity.[17,18,20,27–29] The artificially-introduced viscosity or its equivalent causes a dissipation meant to ensure the stable numerical solution. As a side effect, that leads to non-uniform distribution of entropy and temperature near interfaces after the shock wave propagation. These non-uniformities are absent in an analytical solution for ideal hydrodynamics, therefore, they are treated as shortcomings of the obtained numerical solution. Non-physical nature of such artificial entropy traces is confirmed by their strong dependence on the numerical mesh size. As opposed to heating error, here we communicate about the physical effect caused by real dissipation processes, plasticity, first of all. To exclude the mentioned numerical effect we completely exclude the artificial viscosity, as in Refs. 17, 18 or 20, and accounts only physical, mesh-independent, viscosity and plasticity. The resulting numerical solution is stable if computational grid is

fine enough, that means, if the compression wave front is resolved properly.[20]

The work structure is as follows. Basic relations of entropy rise in fluids and solids are considered in Sec. II. A mathematical model we used is described in Sec. III. Details of a numerical implementation of the model are presented in Sec. IV. Numerical stability and high-entropy layers in shock-loaded fluids are analyzed in Sec. V. High-entropy layers in solid metals behind shock waves are investigated in Sec. VI. Non-isentropic layers at ramp loading are studied in Sec. VII. Interaction of shock waves with interfaces is regarded in Sec. VIII. Finally, our conclusions are summarized in Sec. IX.

II. ENTROPY RISE IN FLUIDS AND SOLIDS

As is well-known, the entropy remains constant only in equilibrium adiabatic processes, which should be very slow.[30] Non-equilibrium leads to the entropy rise: the higher strain rate, the greater degree of non-equilibrium, the higher entropy rise. Different dissipative processes are the particular mechanisms of such entropy rise.

Viscosity is the most obvious mechanism of dissipation in fluids. At uniaxial compression or tension of a fluid, the strain rate equals to $\dot{\varepsilon} = \partial\upsilon/\partial z$, where υ is the particle velocity and z is the coordinate. Viscous stress is equal to[31]

$$\sigma'_{zz} = \left(\frac{4\eta}{3} + \zeta\right)\frac{\partial\upsilon}{\partial z} = \left(\frac{4\eta}{3} + \zeta\right)\dot{\varepsilon},$$

where η is the shear viscosity coefficient, ζ is the bulk viscosity coefficient. The dissipating power per unit volume is equal to

$$\sigma'_{zz}\frac{\partial\upsilon}{\partial z} = \left(\frac{4\eta}{3} + \zeta\right)\dot{\varepsilon}^2.$$

This power leads to the heat release and the entropy rise with the rate

$$\frac{\mathrm{d}s}{\mathrm{d}t} = \left(\frac{4\eta}{3} + \zeta\right)\frac{\dot{\varepsilon}^2}{\rho T}, \tag{1}$$

where ρ is the substance density, T is the temperature, s is the specific entropy. Rate of density change is equal to $\mathrm{d}\rho/\mathrm{d}t = -\rho\dot{\varepsilon}$, from which we obtain the following derivative

$$\frac{\mathrm{d}s}{\mathrm{d}\rho} = -\left(\frac{4\eta}{3} + \zeta\right)\frac{\dot{\varepsilon}}{\rho^2 T}. \tag{2}$$

Thus, a small density increment $\mathrm{d}\rho$ leads to the specific entropy increment $\mathrm{d}s$, which is proportional to the strain rate. So, the higher strain rate, the larger entropy rise, at the same final compression ratio.

The entropy jump on a steady shock-wave front is determined only by substance parameters on either side of the shock discontinuity that means, by the Hugoniot relation. In turn, the shock-wave thickness and the strain rate on its front are determined by the entropy jump and the substance coefficient of viscosity. The shock-wave profile becomes steady not instantly after impact: as was mentioned above, an initial velocity gradient (strain rate) is formally infinite on the interface between the colliding bodies. Although the gradient value should be physically restricted by various imperfections of the contacting surfaces or by the atomic structure of substance, nevertheless, the initial velocity gradient on the interface is higher than on the steady shock front. Therefore, as it follows from Eq. (2), the substance near the impact surface should be heated more than immediately behind the steady shock front. It is the physical reason of the high-entropy layer formation near the impact surface in a viscous fluid or similar matter with dissipation.

Similar situation takes place in solids, where an additional dissipation mechanism appears that is the plasticity. Experiments and simulations[8] on the powerful ultra-short laser irradiation of thin metal foils show that the elastoplastic properties of substance reveal themselves even in the shock waves with the pressure jump of several tens of gigapascals, at least at small target thicknesses. The high-entropy layer structure can be essential for such thin targets.

The dissipating power due to the plastic deformation per unit volume is determined by the product $S_{ik}\dot{w}_{ik}$, where S_{ik} are the components of stress deviator, w_{ik} are the components of the plastic strain tensor and $\dot{w}_{ik}$ are their time derivatives; the Einstein summation convention is used. This product takes the following form at the one-dimensional deformation, which is typical for plate impact or ramp loading:

$$S_{ik}\dot{w}_{ik} = \frac{3}{2}S_{zz}\dot{w}_{zz},$$

where the relations $S_{xx} = S_{yy} = -S_{zz}/2$ and $w_{xx} = w_{yy} = -w_{zz}/2$ are used, than the entropy rise rate is

$$\frac{\mathrm{d}s}{\mathrm{d}t} = \frac{3}{2\rho}S_{zz}\dot{w}_{zz}. \tag{3}$$

The plastic strain rate $\dot{w}_{zz}$ is proportional to the dislocations velocity according to the

well-known Orowan equation, while the dislocation velocity is approximately proportional to the shear stresses in the over-barrier gliding mode.[32–34] Therefore, one can write $\dot{w}_{zz} = KS_{zz}$, where K is a coefficient of proportionality depending on the dislocations subsystem state, and, inversely, $S_{zz} = K^{-1}\dot{w}_{zz}$. This proportionality is disturbed at high values of the dislocation velocity, because the latter is bounded above by the transverse velocity of sound.[33,35] The plastic strain should completely balance the external deformation and prevent the shear stress rise at the steady plastic flow; then one can write $\dot{w}_{zz} = 2\dot{\varepsilon}/3$ (in particular, that can be obtained from expressions of Ref. 12). In this case, the entropy rise is linearly dependent on the strain rate:

$$\frac{\mathrm{d}s}{\mathrm{d}\rho} = -\frac{2}{3K}\frac{\dot{\varepsilon}}{\rho^2 T}, \tag{4}$$

that is similar to Eq. (2).

Approximation of the ideal fluid (without viscosity and plasticity) is often used at the high-velocity impact modeling. The corresponding equations system is physically incomplete, which leads to instability of its numerical solution. One should use artificial viscosity[36] or its various equivalents to solve this problem. Such artificial dissipation increases the transition layer thickness of a strong discontinuity up to several meshes of the numerical grid. That simulates the physical viscosity, but the simulation results depend on the mesh size (for example, the artificial shock thickness) and consequently are non-physical. This technique seems to be founded for the gas-dynamic processes,[27] in which the physical thickness of shock waves is typically much less than the spatial resolution of the numerical grid. Meanwhile, modeling of the shock waves propagation in the condensed matter is often performed on numerical grid with the mesh size smaller than the shock front thickness. Accounting for the physical viscosity and plasticity and elimination of the artificial those are preferable in this case.[17,18,20] Particularly, it is the way to obtain the physically-based structure of the low- and high-entropy layers near the impact surface.

III. MATHEMATICAL MODEL

We consider a uniaxial deformation of elastoplastic material (metal), which commonly takes place in the field of interest at the shock and ramp loading experiments. In the

framework of continuum mechanics approach, the main equations are the continuity equation

$$\frac{\mathrm{d}\rho}{\mathrm{d}t} = -\rho\frac{\partial \upsilon}{\partial z}, \tag{5}$$

the motion equation

$$\rho\frac{\mathrm{d}\upsilon}{\mathrm{d}t} = \frac{\partial}{\partial z}(-P + S_{zz} + \sigma'_{zz}), \tag{6}$$

and the equation for internal energy

$$\begin{aligned}\rho\frac{\mathrm{d}U}{\mathrm{d}t} \;=\; & (-P + \sigma'_{zz})\frac{\partial \upsilon}{\partial z} \\ & +(1-\alpha)\frac{3}{2}S_{zz}\frac{\mathrm{d}w_{zz}}{\mathrm{d}t} + Q + \frac{\partial}{\partial z}\left(\kappa\frac{\partial T}{\partial z}\right),\end{aligned} \tag{7}$$

where P is the pressure; U is the internal energy; α is the portion of the plastically dissipated energy, which is spent on formation of new dislocations; Q is the energy release due to annihilation of dislocations; κ is the heat conductivity coefficient. Note that the total time derivatives $\mathrm{d}/\mathrm{d}t = \partial/\partial t + \upsilon\partial/\partial z$ are used in Eqs. (5)–(7), which are valid for elements moving with the substance (the Lagrangian frame of reference).

The equation of motion (6) takes account of both the elastic S_{zz} and viscous σ'_{zz} additions to the thermodynamically equilibrium pressure P. The internal energy U does not include the elastic energy of the shape change (shear deformations and stresses) and the energy of defects (dislocations). This means that U corresponds to a body with the same density and temperature, but without any shear stresses and without structural defects. The second term in the right-hand part of Eq. (7) takes into account the heating at plastic deformation, similar to Eq. (3). At the same time, the elastic addition S_{zz} is not included in the first term of the right-hand part of Eq. (7); otherwise that should lead to overestimation of the plastic heating. Summand $S_{zz}(\partial\upsilon/\partial z)$ pumps the elastic energy of the shape change at first, then the main part of this energy are transforming into the internal energy U in the course of plastic deformation including annihilation of dislocations. This sequence of processes is reflected in Eq. (7). The last term in the right-hand part of Eq. (7) accounts for the heat conduction.

Viscous stress is determined by a simple relation[31]

$$\sigma'_{zz} = \eta^*\frac{\partial \upsilon}{\partial z}, \tag{8}$$

where $\eta^* = 4\eta/3 + \zeta$ is the coefficient of viscosity for the considered one-dimensional deformation.

Wide-range equations of state for metals[37] are used to determine the pressure $P = P(\rho, U)$ and the temperature $T = T(\rho, U)$ as functions of density and internal energy calculated from Eqs. (5) and (7) correspondingly. In the hydrodynamic approximation one should set $S_{zz} = 0$ and $w_{zz} = 0$, and then Eqs. (5)–(8) together with the equation of state form a closed system. In the elastoplastic approach one should define additional equations for the plastic strain and stress deviator instead. For description of the elastoplastic properties, we use the dislocation plasticity model proposed in Refs. 12 and 26 as described below.

Here we make calculations only for fcc monocrystalline metals (copper and aluminum) loaded in [100] direction. In this situation, stress and strain fields are symmetrical with respect to axial rotation, and diagonal elements of the stress deviator and the plastic strain tensor satisfy the relations $S_{xx} = S_{yy} = -S_{zz}/2$ and $w_{xx} = w_{yy} = -w_{zz}/2$, while all non-diagonal elements are equal to zero. These are already taken into account in Eq. (7). The stress deviator component S_{zz} is calculated from the Hook's law:[38]

$$S_{zz} = 2G\left(\frac{2}{3}u_{zz} - w_{zz}\right), \tag{9}$$

where G is the shear modulus; u_{zz} is the component of the macroscopic strain tensor, the time derivative of u_{zz} is determined by the velocity of the macroscopic motion of matter:[12]

$$\frac{\mathrm{d}u_{zz}}{\mathrm{d}t} = \frac{\partial \upsilon}{\partial z}. \tag{10}$$

The shear modulus is taken linearly increasing with pressure and linearly decreasing with temperature for both considered metals:

$$G(T, P) = G_0 + G'_P P + G'_T (T - T_0), \tag{11}$$

where $T_0 = 300$ K; G_0 is the shear modulus at normal conditions; the values of pressure derivative G'_P and temperature derivative G'_T are taken from Ref. 39 and listed in Table I.

The plastic strain rate can be calculated from the generalized Orowan equation:[32]

$$\frac{\mathrm{d}w_{zz}}{\mathrm{d}t} = \sum_{\beta} b_z^{\beta} n_z^{\beta} V_{\mathrm{D}\beta} \rho_{\mathrm{D}\beta}, \tag{12}$$

where index β numerates the slip systems of dislocations (the groups of dislocations);[12,26] b_z^{β} is the component of Burgers vector and n_z^{β} is the component of unit vector normal to the slip plane; $V_{\mathrm{D}\beta}$ is the velocity of moving dislocations relative to substance and $\rho_{\mathrm{D}\beta}$ is the

scalar density of dislocations (the total length of dislocations of the corresponding group per unit volume of substance).

The slip systems are determined by the crystal structure of specified metal; there are 12 different slip systems in the considered fcc metals,[40] those are listed in Table II. In the case of [100] loading, the lab coordinates coincides with the crystallographic coordinates. As one can see, four slip systems make zero contribution in the plastic strain because of $b_z^\beta = 0$, while the other eight slip systems make equal contribution because $b_z^\beta n_z^\beta = 6^{-1/2} b$ for all of them. Therefore, a simpler form of Eq. (12) can be used at such loading conditions:

$$\frac{\mathrm{d}w_{zz}}{\mathrm{d}t} = \frac{b}{\sqrt{6}} V_\mathrm{D} \rho_\mathrm{D}, \tag{13}$$

where ρ_D is the total scalar density of dislocation in all eight active slip systems; V_D is the moving dislocation velocity in the active slip systems. The modulus of Burgers vector b in the compressed substance can be calculated from the density ρ; for fcc crystals one can obtain:

$$b = \frac{1}{\sqrt{2}} \left(\frac{4\mu}{\rho N_\mathrm{A}} \right)^{1/3}, \tag{14}$$

where μ is the molar mass; N_A is the Avogadro constant.

Velocity of moving dislocations is determined by the macroscopic shear stresses[32] characterized by S_{zz}. In the considered case, the equation of dislocation motion[12,35] takes the following form:

$$\begin{aligned} m_0 \frac{\mathrm{d}V_\mathrm{D}}{\mathrm{d}t} \; = \; & \frac{b[1 - (V_\mathrm{D}/c_t)^2]^{3/2}}{2} \left[\sqrt{\frac{3}{2}} S_{zz} - Y \,\mathrm{sign}\,(S_{zz}) \right] \\ & - B V_\mathrm{D}, \end{aligned} \tag{15}$$

where $m_0 = \rho b^2$ is the rest mass of dislocations per unit length; Y is the static yield strength; B is the drag coefficient. The motion of dislocations and the corresponding plastic deformation take place only if $|S_{zz}| > Y\sqrt{2/3}$. The first term in the right-hand part of Eq. (15) includes a quasi-relativistic multiplier,[35] which reflects the fact that the dislocation velocity is restricted above by the transverse velocity of sound $c_t = \sqrt{G/\rho}$.

The phonon drag is the most important in the temperature range of interest.[34,41] The following temperature dependence can be written for the drag coefficient:[34]

$$B = \frac{4\theta^2 k_\mathrm{B}^3}{h^2 c_b^3} T, \tag{16}$$

where k_B is the Boltzmann constant; h is the Planck constant; θ is the parameter with the dimensionality of temperature (see Table I); c_b is the bulk velocity of sound, which is defined from the equation of state.[37] The yield strength is determined by the Taylor relation:[34]

$$Y = Y_0 + A_\mathrm{I} G b \sqrt{\rho_\mathrm{I}}, \tag{17}$$

where Y_0 includes resistance from point obstacles and Peierls barrier and the second term accounts interaction between moving dislocations and immobilized one; A_I is the constant of interaction and ρ_I is the total density of immobilized dislocations.[12] Accounting of immobilized dislocations allows one to get a good fit with experimental profile of unloading wave.[12]

The kinetics equations[12] for mobile and immobilized dislocations are as follows:

$$\frac{\mathrm{d}\rho_\mathrm{D}}{\mathrm{d}t} = Q_\mathrm{D} - Q_\mathrm{I} - Q_\mathrm{Da} + \frac{\rho_\mathrm{D}}{\rho}\frac{\mathrm{d}\rho}{\mathrm{d}t}, \tag{18}$$

$$\frac{\mathrm{d}\rho_\mathrm{I}}{\mathrm{d}t} = Q_\mathrm{I} - Q_\mathrm{Ia} + \frac{\rho_\mathrm{I}}{\rho}\frac{\mathrm{d}\rho}{\mathrm{d}t}, \tag{19}$$

where Q_D is the generation rate of the mobile dislocations; Q_I is the rate of immobilization; Q_Da and Q_Ia are the annihilation rates of mobile and immobilized dislocations correspondingly:

$$Q_\mathrm{Da} = k_\mathrm{a} b |V_\mathrm{D}| \rho_\mathrm{D} (2\rho_\mathrm{D} + \rho_\mathrm{I}), \tag{20}$$

$$Q_\mathrm{Ia} = k_\mathrm{a} b |V_\mathrm{D}| \rho_\mathrm{D} \rho_\mathrm{I}, \tag{21}$$

where k_a is the annihilation factor.

The last terms in Eqs. (18) and (19) take into account the dislocation density change due to compression or tension of substance. The rate of generation is as follows:

$$Q_\mathrm{D} = \frac{\alpha}{\varepsilon_\mathrm{D}} \left\{ \frac{B V_\mathrm{D}^2}{[1 - (V_\mathrm{D}/c_t)^2]^{3/2}} + \frac{b}{2} Y |V_\mathrm{D}| \right\} \rho_\mathrm{D}, \tag{22}$$

where $\varepsilon_\mathrm{D} \approx 8$ eV$/b$ is the energy of the dislocations formation per unit length.[42] The multiplier in curly brackets in Eq. (22) is the energy dissipation rate per unit length of dislocation; this is the sum of the work against the phonon friction and the work against the resistance force.[35] The part of dissipated energy α spent on formation of new dislocations is an important parameter of the model; the value $\alpha = 0.1$ is used (see Table I), which follows from calorimetric measurements at small plastic deformations.[42] If one neglects the kinetic energy

of dislocations $\rho_{\rm D} m_0 V_{\rm D}^2/(2\rho) = \rho_{\rm D} V_{\rm D}^2 b^2/2 \approx 10$ J/kg, then the rate (22) takes a simple form:

$$Q_{\rm D} = \frac{\alpha}{\varepsilon_{\rm D}} \left(\frac{3}{2} S_{zz} \frac{{\rm d}w_{zz}}{{\rm d}t} \right). \tag{23}$$

The rate of immobilization is as follows:

$$Q_{\rm I} = V_{\rm I}(\rho_{\rm D} - \rho_0)\sqrt{\rho_{\rm I}}. \tag{24}$$

The latter equation describes the immobilization process, where parameter ρ_0 is the minimal dislocations density, which is necessary for their consolidation and immobilization in dislocation structures.[12] This expression is written from the assumption that all excess mobile dislocations will be immobilized in structures with the characteristic time $\tau_{\rm I} \approx r_{\rm I}/V_{\rm I}$, where $r_{\rm I} \approx (\rho_{\rm I})^{-1/2}$ is the average distance between the immobile dislocations. Parameter $V_{\rm I}$ means a characteristic velocity of the dislocations movement during the process of consolidation; that is determined by internal stresses.

The substance heating rate Q due to annihilation of dislocations can be expressed as

$$Q = \varepsilon_{\rm D}(Q_{\rm Da} + Q_{\rm Ia}). \tag{25}$$

So, we have formulated the closed system of equations for description of elestoplastic deformation of fcc metals on the basis of dislocations dynamics and kinetics.[12,26] Main equations are Eqs. (5)–(10), (13), (15), (18) and (19). The verified model parameters are listed in Table I.

IV. NUMERICAL IMPLEMENTATION

In the considered problem, one should clearly differentiate between the physical and numerical effects; therefore, here, a large attention is devoted to the description of the numerical implementation. The four physical processes are separated to simplify the problem: (i) the motion of a substance according to Eqs. (5)–(8) and (10) with the reduced Eq. (7) without heat conduction and plastic heating; (ii) the kinetics of dislocations and plastic deformation by Eqs. (13), (15), (18) and (19) with auxiliary relations and the plastic heating in Eq. (7); (iii) the heat conductivity from Eq. (7); (iv) determination of the thermodynamic state from the equation of state[37] and calculation of shear stress in accordance with Eq. (9). Contributions of the processes (i)–(iii) are calculated sequentially at every time step. At numerical

discretization, the substance velocities and coordinates are defined in the mesh points and numerated by the integer subscripts $\{i\}$, while all other quantities, including the thermodynamic parameters and dislocation characteristics, are defined in the centers of meshes and numerated by the half-integer subscripts $\{i+1/2\}$. The time layers are numerated by the integer superscripts (n). The Lagrangian frame of reference is used as it is mentioned in the previous section.

Accounting for the physical viscosity, Eq. (8), lets one to obtain the stable numerical solution for the process (i) even by using of the simple explicit Euler method. Equation of motion (6) leads to the following relation:

$$\begin{aligned} \upsilon_{\{i\}}^{(n+1)} &= \upsilon_{\{i\}}^{(n)} + \Big((-P + S_{zz} + \sigma'_{zz})_{\{i+1/2\}}^{(n)} \\ &\quad -(-P + S_{zz} + \sigma'_{zz})_{\{i-1/2\}}^{(n)}\Big)\frac{\Delta t}{m_{\{i\}}}, \end{aligned} \tag{26}$$

where $\Delta t = t^{(n+1)} - t^{(n)}$ is the time step;

$$m_{\{i\}} = \frac{m_{\{i+1/2\}} + m_{\{i-1/2\}}}{2},$$

$$m_{\{i+1/2\}} = \rho_{\{i+1/2\}}^{(n)} V_{\{i+1/2\}}^{(n)}$$

is the substance mass in the mesh, that is constant during the substance motion;

$$V_{\{i+1/2\}}^{(n)} = z_{\{i+1\}}^{(n)} - z_{\{i\}}^{(n)}$$

is the mesh volume. New position of the mesh points are calculated from the following expression:

$$z_{\{i\}}^{(n+1)} = z_{\{i\}}^{(n)} + \Big(\upsilon_{\{i\}}^{(n+1)} + \upsilon_{\{i\}}^{(n)}\Big)\frac{\Delta t}{2}. \tag{27}$$

Equation for internal energy (7) gives one:

$$\begin{aligned} \tilde{\tilde{U}}_{\{i+1/2\}}^{(n+1)} &= U_{\{i+1/2\}}^{(n)} + \frac{\Delta V_{\{i+1/2\}}}{m_{\{i+1/2\}}} \\ &\quad \times(-P + S_{zz} + \sigma'_{zz})_{\{i+1/2\}}^{(n)}, \end{aligned} \tag{28}$$

where

$$\Delta V_{\{i+1/2\}} = V_{\{i+1/2\}}^{(n+1)} - V_{\{i+1/2\}}^{(n)}$$

is the mesh volume change over the time step. Relation (28) does not take into account the internal energy change due to the plastic heating and the heat conduction on the stage (i).

The substance density can be calculated from the mesh volume:

$$\rho_{\{i+1/2\}}^{(n+1)} = \frac{m_{\{i+1/2\}}}{V_{\{i+1/2\}}^{(n+1)}}. \tag{29}$$

Approximation of the viscous stress, Eq. (8), is as follows:

$$(\sigma'_{zz})_{\{i+1/2\}}^{(n+1)} = \eta^* \frac{v_{\{i+1\}}^{(n+1)} - v_{\{i\}}^{(n+1)}}{V_{\{i+1/2\}}^{(n+1)}}, \tag{30}$$

and relation for the macroscopic strain, Eq. (10), gives:

$$(u_{zz})_{\{i+1/2\}}^{(n+1)} = (u_{zz})_{\{i+1/2\}}^{(n)} + \frac{\Delta z_{\{i+1\}} - \Delta z_{\{i\}}}{V_{\{i+1/2\}}^{(n+1)}}, \tag{31}$$

where

$$\Delta z_{\{i\}} = z_{\{i\}}^{(n+1)} - z_{\{i\}}^{(n)}$$

is the mesh point displacement over the time step.

The time step for process (i) is chosen from Courant–Friedrichs–Lewy condition:

$$\Delta t = 0.05 \min_i \frac{2\left|z_{\{i+1\}}^{(n)} - z_{\{i\}}^{(n)}\right|}{2(c_l)_{\{i+1/2\}}^{(n)} + \left|v_{\{i+1\}}^{(n)}\right| + \left|v_{\{i\}}^{(n)}\right|}, \tag{32}$$

where $c_l = \sqrt{c_b^2 + 4G/(3\rho)}$ is the longitudinal sound velocity. The same time step is used at the numerical solution for stages (ii) and (iii).

The process (ii) does not include any spatial transfer and all equations are local: ranges of dislocations are supposed to be negligibly short. Equation for the dislocations velocity (15) is the most problematic in the block (ii) due to the quasi-relativistic factor and low rest mass of dislocation. Therefore, the interpolating analytic solution[35] is used instead of the precise one:

$$\begin{aligned}(V_{\mathrm{D}})_{\{i+1/2\}}^{(n+1)} \;=\; & (V_{\mathrm{D}})_{\{i+1/2\}}^{(n)} \mathrm{e}^{-\Delta t/\tau} \\ & + V_\infty \Big(1 - \mathrm{e}^{-\Delta t/\tau}\Big),\end{aligned} \tag{33}$$

where

$$V_\infty = \frac{1}{6\sqrt{6\chi\xi}} \Big(\xi^{2/3} - 12\Big)^{3/2} (c_t)_{\{i+1/2\}}^{(n)},$$

$$\chi = \left(\frac{b}{2c_t B} \left[\sqrt{\frac{3}{2}} S_{zz} - Y \operatorname{sign}(S_{zz}) \right] \right)_{\{i+1/2\}}^{(n)},$$

$\xi = 108\chi + 12\sqrt{12 + 81\chi^2}$, and the inverse characteristic time

$$\frac{1}{\tau} = \left(\frac{B}{m_0} + \frac{b}{2c_t m_0} \left[\sqrt{\frac{3}{2}} S_{zz} - Y \,\mathrm{sign}\,(S_{zz}) \right] \right)^{(n)}_{\{i+1/2\}}.$$

Equations for scalar density of mobile (18) and immobilized (19) dislocations are solved by the explicit Euler method:

$$\begin{aligned} (\rho_{\mathrm{D}})^{(n+1)}_{\{i+1/2\}} &= (\rho_{\mathrm{D}})^{(n)}_{\{i+1/2\}} \sigma^{(n+1/2)}_{\{i+1/2\}} \\ &\quad + (Q_{\mathrm{D}} - Q_{\mathrm{I}} - Q_{\mathrm{Da}})^{(n)}_{\{i+1/2\}} \Delta t, \end{aligned} \tag{34}$$

$$\begin{aligned} (\rho_{\mathrm{I}})^{(n+1)}_{\{i+1/2\}} &= (\rho_{\mathrm{I}})^{(n)}_{\{i+1/2\}} \sigma^{(n+1/2)}_{\{i+1/2\}} \\ &\quad + (Q_{\mathrm{I}} - Q_{\mathrm{Ia}})^{(n)}_{\{i+1/2\}} \Delta t, \end{aligned} \tag{35}$$

where the ratio

$$\sigma^{(n+1/2)}_{\{i+1/2\}} = \frac{V^{(n)}_{\{i+1/2\}}}{V^{(n+1)}_{\{i+1/2\}}}$$

takes into account the substance compression or tension according to the last terms in Eqs. (18) and (19). Equation for the plastic strain (13) is integrated similarly:

$$\begin{aligned} (w_{zz})^{(n+1)}_{\{i+1/2\}} &= (w_{zz})^{(n)}_{\{i+1/2\}} \\ &\quad + (b V_{\mathrm{D}} \rho_{\mathrm{D}})^{(n)}_{\{i+1/2\}} \frac{\Delta t}{\sqrt{6}}. \end{aligned} \tag{36}$$

Correction of the internal energy accounted for the heating at plastic deformation is as follows:

$$\begin{aligned} \tilde{U}^{(n+1)}_{\{i+1/2\}} &= \tilde{\tilde{U}}^{(n+1)}_{\{i+1/2\}} + Q^{(n)}_{\{i+1/2\}} \Delta t + (1-\alpha) \\ &\quad \times \frac{3}{2} (S_{zz})^{(n)}_{\{i+1/2\}} (\Delta w_{zz})_{\{i+1/2\}}, \end{aligned} \tag{37}$$

where

$$(\Delta w_{zz})_{\{i+1/2\}} = (w_{zz})^{(n+1)}_{\{i+1/2\}} - (w_{zz})^{(n)}_{\{i+1/2\}}$$

is the plastic strain increment over the time step.

Explicit integration is also used for the heat conductivity process (iii). The internal energy from Eq. (37) is corrected and the final value is obtained as

$$U^{(n+1)}_{\{i+1/2\}} = \tilde{U}^{(n+1)}_{\{i+1/2\}} - \frac{q^{(n)}_{\{i+1\}} - q^{(n)}_{\{i\}}}{z^{(n)}_{\{i+1\}} - z^{(n)}_{\{i\}}} \frac{\Delta t}{\rho^{(n)}_{\{i+1/2\}}}, \tag{38}$$

where the heat flux through the mesh boundary is

$$q^{(n)}_{\{i\}} = -\left(\kappa^{(n)}_{\{i+1/2\}} + \kappa^{(n)}_{\{i-1/2\}}\right) \frac{T^{(n)}_{\{i+1/2\}} - T^{(n)}_{\{i-1/2\}}}{z^{(n)}_{\{i+1\}} - z^{(n)}_{\{i-1\}}}. \tag{39}$$

Temperature dependence of the heat conductivity coefficient is taken in tabular form from Ref. 43.

Stage (iv) is the implementation of the constitutive relations. The equation of state was realized as tabulated functions $P = P(\rho, T)$, $U = U(\rho, T)$ and others.[44] Using appropriate subroutines for search and interpolation of tabular data[44] let one to determine the temperature, pressure and bulk sound velocity from the known density via Eq. (29) and internal energy via Eqs. (28), (37) and (38). Then the new value of shear modulus can be calculated from Eq. (11), and the new value of stress deviator is followed from the Hook law, Eq. (9):

$$(S_{zz})^{(n+1)}_{\{i+1/2\}} = 2G^{(n+1)}_{\{i+1/2\}} \left(\frac{2}{3}u_{zz} - w_{zz}\right)^{(n+1)}_{\{i+1/2\}}. \tag{40}$$

V. NUMERICAL STABILITY AND HIGH-ENTROPY LAYERS IN FLUIDS

We solve numerically the problem, which is equivalent to symmetric collision of metal plates. One of the plates is under consideration, which moves along the oZ axis with the initial velocity $-u$. Left boundary $z = 0$ of the plate is at rest, while its right boundary is free. Substance deceleration at the left boundary forms a shock wave spreading to the right; the total velocity jump on the shock wave is equal to u. In this section, a solution is done in hydrodynamic approximation; that means a viscous fluid is considered with thermodynamic properties similar to the metal.

The numerical experiments have shown that solution is unstable for non-viscous fluid (at $\eta^* = 0$): strong oscillations of parameters take place behind the shock wave front. In viscous fluid (at $\eta^* > 0$), the viscosity stabilizes the solution and widens the shock front. Dependence of the shock front thickness $h_{\rm SW}$ upon the coefficient of viscosity η^* and the velocity jump u has been numerically investigated. The shock front thickness is calculated as a distance between two points corresponding to the substance velocity change from its initial value on the magnitude of $\Delta v/u = 0.1$ and 0.9. The obtained results correspond to the relation that follows from the dimensional considerations:

$$h_{\rm SW} = A\frac{\eta^*}{\rho_0 u}, \tag{41}$$

where ρ_0 is the initial substance density, A is dimensionless coefficient of the order of unity: $A \approx 1.3$ for copper and $A \approx 1.4$ for aluminum.

The numerical solution is stable if the shock front layer is described by no less than 3 mesh points of the computational grid:

$$h_{\mathrm{SW}} \geqslant 3\Delta z, \tag{42}$$

where Δz is the mesh size. The condition (42) can be always satisfied by choosing of the fine enough grids. Therefore, a stable solution can be obtained at arbitrary small viscosity coefficient η^* if the computational grid is detailed enough to describe the shock wave structure. The solution is unstable at large values of viscosity η^* if the shock front thickness h_{SW} becomes comparable with the size of the entire computational domain. The numerical experiments show that the shock front thickness tends to zero if the viscosity coefficient tends to zero, in accordance with Eq. (41).

The spatial distributions of the substance temperature, calculated in the model formulation (excluding thermal conductivity, $\kappa = 0$) are shown in Fig. 1a for Al; velocity jump is $u = 1$ km/s. The initial temperature value is $T_0 = 300$ K; the temperature behind the steady shock wave is $T_{\mathrm{SW}} \approx 470$ K; the substance temperature near the collision surface is higher, $T > T_{\mathrm{SW}}$: the high-entropy layer takes place. We observe this as the layer of higher temperature, but call that by the high-entropy layer because the entropy is commonly considered as the measure of non-equilibrium, which is the cause of the layer formation. The substantial temperature increase in comparison with T_{SW} takes place on distances about h_{SW} from the collision surface ($h_{\mathrm{SW}} \approx 0.6$ μm in the considered case). Numerical solution is at the limit of stability for the mesh size $\Delta z = 0.2$ μm according to the condition of Eq. (42).

The total thickness of the high-entropy layer is independent on the mesh size; that is determined only by the viscosity coefficient. The high-entropy layer profile (particularly the temperature distribution on spatial coordinate) on the distances higher than h_{SW} from the collision surface is also independent on the mesh size. These are attractive properties of the obtained numerical solution distinguishing that from the heating errors (or entropy tracks) produced by artificial viscosity, as mentioned in Sec. I. It is evident from Fig. 1a that a strong dependence of the temperature near the collision surface on the mesh size takes place. Difference approximation of the strain rate is limited by the value of the order of $|\dot{\varepsilon}| < u/\Delta z$; therefore, the strain rate, the entropy and temperature near the collision

surface are increasing with the decrease of Δz, nearly inversely to Δz in accordance with Eq. (2). In the circumstances, an unlimited decrease of the mesh size leads to unlimited rise of temperature.

The calculation results with taking into account the heat conductivity are shown in Fig. 1b. The temperature near the collision surface is substantially lower than in the above-mentioned calculations illustrated by Fig. 1a, and that is not tend to infinity at $\Delta z \to 0$, quite the contrary, that converges to a finite limit, $T \approx 550$ K in the case. The heat conductivity also leads to the smearing of the high entropy layer with time.

A stable profile of the high-entropy layer independent on the mesh size can be obtained only with use of very fine computational grid ($\Delta z \approx 0.01$ μm in the considered case). It should be noted that perturbations of flow induced by non-parallelism or roughness of the impacting surfaces can influence on the high-entropy layer formation in the real conditions. Therefore, using of unreasonably fine grids can be senseless for most of the problems, for example, using of the mesh size Δz less than the surface roughness.

According to data from Refs. 45 and 46, the shear viscosity of Al melt is about $\eta \sim 10^{-2}$ Pa·s under normal pressure, while according to Ref. 47 it is even less, $\eta \sim 10^{-3}$ Pa·s. Our simulations show that the stable solutions can be obtained at such low value of the viscosity coefficient $\eta^* \sim 10^{-2}$ Pa·s, but with very small mesh size $\Delta z \approx 0.01$ μm. On the other hand, viscosity depends on pressure and temperature and, according to some estimations, can growth on orders of magnitude with the presuure increase on tens of gigapascals.[48] Moreover, there is additional bulk viscosity ζ, which contribute to the total dissipation in Eqs. (2) and (8), but there is no information about its value. Obviously, the pressure-dependent shear and bulk viscousities of metals should be subjects for further investigations. In the present study, we use the viscosity coefficient as a parameter of calculations; this approach is validated in the next section.

VI. HIGH-ENTROPY LAYERS IN SOLID METALS

Like in the previous section ($\eta^* > 0$, $\kappa > 0$), here we solve the problem of symmetric collision of metal plates but with taking into account elastoplastic properties of the material. The shock wave moves to the right from the collision surface; the substance behind the shock front is at rest, while the substance before the shock front moves to the left with velocity

$-u$; velocity jump on the shock front equals u.

Comparison of results for symmetric collision of aluminum plates calculated in hydrodynamic and elastoplastic approximations on numerical grid with the mesh size of $\Delta z \approx 0.1$ μm is made in Fig. 2. The viscosity coefficient is $\eta^* = 1$ Pa $\cdot$ s, which value is enough to stabilize the numerical solution but weakly influence on the resulting temperature distribution. Accounting for the elastoplastic properties results in the separation of a shock wave on the elastic precursor and the main plastic wave.

Far from the collision surface, the stress component, density and temperature behind the shock front tend to the certain constant values, which are nearly the same for both elastoplastic and hydrodynamic calculations. In the case of elastoplastic calculations, the temperature is slightly lower because a part of energy is stored in defects of crystalline structure (dislocations). That contradicts to the data from Ref. 49, where an additional heating due to the plastic dissipation had been reported on the basis of calculations. This additional heating had been proposed[49] as a reason of the higher temperature detected by pyrometric measurements[49,50] in comparison with results of hydrodynamic calculations. We think that the discussed discrepancy is explained by double accounting of the work of deviatoric stress in Ref. 49: the first time in the equation for internal energy and the second time as additional heating due to the plastic work; see our comments to Eq. (7).

Temperature distribution is inhomogeneous near the collision surface (see Fig. 2c) with the maximum on the surface. The high-entropy layers reveal themselves as increasing of temperature (illustrated by Fig. 2c) and decreasing of substance density (see Fig. 2d) near the collision surface $z = 0$ at the constant stress (see Fig. 2a). The high-entropy layer caused by plasticity is wider and more intensive than the corresponding layer in the case of viscous fluid; it means that the accounted physical viscosity weakly influence on the calculation results for the elastoplastic medium. The layer arises in elastoplastic medium due to the higher plastic strain rate near the collision surface in comparison with its value on the steady shock front (see Fig. 2b).

Full width at half maximum of the high-entropy layer is about 16 μm in the case (a half of this width of about 8 μm is shown in Fig. 2 at $z > 0$), that is close to the shock front thickness ($h_{\mathrm{SW}} \approx 11$ μm). At the viscous fluid approximation, one should use the viscosity coefficient of $\eta^* \approx 20$ Pa $\cdot$ s to provide a comparable thickness of the shock wave front, see Eq. (41). The shock front thickness in solids should be determined by both viscosity and

plasticity in general, but determination of physically based values of viscosity coefficient η^* require an additional study as opposed to the plasticity effects, which can be calculated on the basis of self-consistent model.[12,26] In our present calculations, viscosity coefficient is undefined parameter and we tried to make its influence negligible, but that can not be completely excluded because provides stability of a solution. Accounting for the plasticity solely can not provide the stability because that effects not similarly to viscosity. The viscosity makes an additional increase of compressive stresses in the substance elements those are compressing faster than other elements and prevents instability, while plasticity only relaxes the stresses. Therefore, determination of the viscosity coefficient in solids is an important topic for further investigations.

Calculated temperatures on the collision surface $z = 0$ (in 10 ns after the impact) and behind the shock wave front versus the particle velocity and the longitudinal stress jumps on the steady shock wave are shown in Fig. 3. The temperatures difference grows with the shock intensity increase at low stresses and can exceed 1 kK. As the pressure is constant behind the shock front, melting in the high-entropy layer begins at less values of u than after the steady shock wave in the bulk. Aluminum melts near the collision surface at $u > 2.7$ km/s but remains solid in the bulk even at $u = 3.5$ km/s. Subsequent increase of the loading intensity leads to decrease of the temperature difference between the high-entropy layer and the bulk (see Fig. 3); it is because the substance melting in the high-entropy layer prevents further plastic dissipation and corresponding heating. This difference decrease leads to breaks on curves for the collision surface temperature in Fig. 3; these breaks indicate the beginning of melting in the high-entropy layer near the collision surface (just after the impact).

Calculated thickness δ_{ml} of the molten layer near the collision surface that is the thickness of molten part of the high-entropy layer is shown in Fig. 4 as a function of the particle velocity jump u. After the beginning of melting, this thickness linearly grows with u at first, then it becomes equal to the high-entropy layer thickness (about 25 μm) and ceases to grow. Such behavior corresponds to the temperature distribution in the high-entropy layer (see Fig. 2c).

VII. HIGH- AND LOW-ENTROPY LAYERS AT RAMP LOADING

Ramp loading is one of the widespread experimental techniques; it often takes place at laser irradiation, for example. The ramp loading is modeled as a linear increase of pressure

on loaded surface during the rise time τ, after then the pressure is constant:

$$P(t) = \begin{cases} P_{\rm m} t/\tau, & t < \tau, \\ P_{\rm m}, & t \geqslant \tau, \end{cases} \tag{43}$$

where $P_{\rm m}$ is the maximal acting pressure. A metal plate is considered; the front surface is loaded, while the rear surface is free; the substance is at rest initially.

Temperature fields near the loaded surface are presented in Fig. 5 for the case of aluminum loading with the maximal pressure $P_{\rm m} = 15$ GPa. Various rise times are considered; zero rise time corresponds to the shock loading (like at the plate impact). At any loading rise time, an initially unsteady compression wave transforms into the steady shock wave with time. After this transformation, the temperature behind the compression wave becomes constant (the steady shock wave level in Fig. 5). Near the loaded surface the temperature is higher or lower than the steady shock wave level, so the high-entropy or low-entropy layers are formed depending on the rise time. If the rise time is small, initial strain rate is higher than on the steady shock front and the high-entropy layer is formed; limiting case $\tau = 0$ corresponds to the results of previous section. On the contrary, large rise time leads to a lower initial value of the strain rate and the low-entropy layer is formed; this situation is more common for the ramp loading. The rise time $\tau = 3$ ns is approximately equal to the thickness (in time units) of the steady shock front, and almost flat temperature distribution is formed as a result (see Fig. 5).

Results of hydrodynamic calculations are also presented in Fig. 5 for comparison. In the hydrodynamic calculations, the temperature tends to the Hugoniout adiabat level far from the loaded surface, as well as it tends to the Poisson adiabat level near the loaded surface with increase of the rise time τ. The temperature behind the steady shock for elastoplastic calculations is slightly lower than in the hydrodynamic approximation and than the Hugoniot adiabat level due to expenditure of energy on the formation of new dislocations, as it is mentioned in the previous section. Near the loaded surface, the temperature is, vise versa, higher for the elastoplastic calculations due to additional dissipation mechanism.

The rise time dependence of the loaded surface temperature is presented in Fig. 6. It is monotonically decreasing with the maximal value corresponding to the zero rise time. This dependence crosses the Hugoniot adiabat level at $\tau \approx 3$ ns and tends to the Poisson adiabat level with increase of the rise time; thus, compression in the low-entropy layer becomes close

to the isentropic one at $\tau \to 0$.[15,17,18] Extension of the rise time also increases the thickness of the low-entropy layer.

VIII. SHOCK WAVE INTERACTION WITH INTERFACES

Non-uniform distribution of temperature can be expected near various interfaces after the shock wave interaction with them. The reason is the evolution of the shock (or release) wave structure at crossing of the interface. At the evolution, the strain rate, the entropy production and the heating vary from point to point.

The temperature field near the rear free surface of aluminum plate after reflection of the shock wave with velocity jump $u = 2$ km/s is shown in Fig. 7. Far from the rear surface, the temperature tends to a constant level corresponding to the action of steady shock and release waves. Near the surface the distribution of temperature is considerably inhomogeneous. It has a maximum on depth of about 12 μm from the rear surface with temperature increase about 50 K in comparison with deeper layers, while on the surface itself the temperature drops on about 300 K. This temperature drop occurs because the surface layer does not undergo the complete compression as the deeper layers do: due to the finite thickness of the shock front, unloading starts here before the compression is finished. Thus, the low-entropy layer is formed mainly, while the high-entropy layer (near the temperature maximum) is also exists. The last one is formed during the evolution of the unloading wave structure.

Interaction of the shock wave with interface between two different materials is illustrated in Figs. 8 and 9 by the example of copper and aluminum. The case of Fig. 8 corresponds to the shock wave crossing from harder material into the softer one, where the reflection of unloading wave happens. While in the case of Fig. 9, the harder and softer materials are interchanged, and the reflection of shock wave takes place. Temperatures far from the interface correspond to the action of steady shock and release waves. Near the interface the low-entropy layer is formed in the harder material (Cu), and the high-entropy layer is formed in the softer material (Al). Structure of these layers can be more complicated than at the considered above shock or ramp loading.

Existence of high- and low-entropy layers near an interface can substantially influence on the pyrometry measurement of temperature as that analyzes radiation from a substance layer near the interface (for example, near free surface or interface between the studied

substance and a window), where the temperature differs from that of bulk.[49] Moreover, the high- and low-entropy layers should be taken into account in such problems, where surface plays an important role, particularly, at loading of thin targets.

IX. CONCLUSIONS

Theoretical analysis and computations show that the non-isentropic layers arise near the collision surface and other interfaces in problems of shock and ramp loading. The cause is the formation or transformation of the steady shock wave structure. At impact, the initial strain rate, entropy production and heating are higher near the collision surface than on the steady shock front; therefore the high-entropy layer is formed. The distance passed by the compression wave after the impact before its conversion into the steady shock wave is comparable with the shock front thickness, which is controlled by viscosity (in fluids and solids) as well as plasticity (in solids). Ramp loading can form the high- or low-entropy layers near the loaded surface in dependence on the pressure rise time, but the low-entropy layer is the most expected. Reflection of the shock wave from a free surface produces a considerable low-entropy (in general) layer near the surface; the particular reason here is that the surface layer does not undergo the complete compression as the substance in the bulk does: unloading starts here before the compression is finished due to the finite thickness of the shock front. At the shock wave crossing the interface between two substances, the low-entropy layer is formed in the higher-impedance material, and the high-entropy layer is formed in the lower-impedance material.

The high- and low-entropy layers should be accurately taken into account at calculations of the thin targets loading and other situations where surface is important. For example, melting can occur in the high-entropy layer, while the substance remains solid behind the steady shock wave deeper in the bulk. Another example is the pyrometry measurements, where the temperature perturbations near the examined surface can affect the result.

For accurate calculations of the mentioned effects, one should exclude artificial viscosity or its analogs from the numerical scheme and use the physically based dissipative processes (the physical viscosity, the plasticity, and the heat conductivity) for stabilization of the solution instead. It is all the more actual since the calculations of the shock-wave processes in condensed matter are commonly performed on the fine numerical grids, which allow one

to resolve the shock wave structure. We use the physical viscosity as a stabilizing factor, but the viscosity coefficient plays a role of parameter of numerical calculations here. Using a fine numerical grid allows one to obtain a stable solution at arbitrary small viscosity coefficient. Plasticity controls the shock wave thickness and the structure of the non-isentropic layers in the considered situations, those justify our approach. In spite of that, the determination of viscosity coefficients in condensed matter is necessary for a physically complete description of the problem.

ACKNOWLEDGMENTS

This work is supported by the President of Russian Federation (grant NSh-6614.2014.2), the Russian Foundation for Basic Research (project 14-08-00967), and the Ministry of Education and Science of Russian Federation (scientific research of Chelyabinsk State University in the framework of competitive part of state assignment 3.1334.2014/K). Authors appreciate greatly Prof. A. A. Charakhchyan, Dr. I. R. Makeyeva, Dr. M. E. Povarnitsyn, Prof. V. F. Kuropatenko, Dr. D. A. Varfolomeyev and Prof. G. I. Kanel for useful discussions.

---

[1] Y. M. Gupta, J. M. Winey, P. B. Trivedi, B. M. LaLone, R. F. Smith, J. H. Eggert, and G. W. Collins, J. Appl. Phys. **105**, 036107 (2009).

[2] J. M. Winey, B. M. LaLone, P. B. Trivedi, and Y. M. Gupta, J. Appl. Phys. **106**, 073508 (2009).

[3] S. Neff, D. Martinez, C. Plechaty, S. Stein, and R. Presura, High Energ. Dens. Phys. **6**, 242 (2010).

[4] S. I. Ashitkov, M. B. Agranat, G. I. Kanel, P. S. Komarov, and V. E. Fortov, JETP Lett. **92**, 516 (2010).

[5] V. H. Whitley, S. D. McGrane, D. E. Eakins, C. A. Bolme, D. S. Moore, and J. F. Bingert, J. Appl. Phys. **109**, 013505 (2011).

[6] R. F. Smith, J. H. Eggert, R. E. Rudd, D. C. Swift, C. A. Bolme, and G. W. Collins, J. Appl. Phys. **110**, 123515 (2011).

[7] S. A. Abrosimov, A. P. Bazhulin, V. V. Voronov, A. A. Geras'kin, I. K. Krasyuk, P. P. Pashinin,

A. Y. Semenov, I. A. Stuchebryukhov, K. V. Khishchenko, and V. E. Fortov, Quantum Electron. **43**, 246 (2013).

[8] N. A. Inogamov, V. V. Zhakhovsky, Y. V. Petrov, V. A. Khokhlov, S. I. Ashitkov, K. V. Khishchenko, K. P. Migdal, D. K. Ilnitsky, Y. N. Emirov, P. S. Komarov, V. V. Shepelev, C. W. Miller, I. I. Oleynik, M. B. Agranat, A. V. Andriyash, S. I. Anisimov, and V. E. Fortov, Contrib. Plasma Phys. **53**, 796 (2013).

[9] S. A. Bel'kov, V. N. Derkach, S. G. Garanin, E. I. Mitrofanov, I. N. Voronich, V. E. Fortov, P. R. Levashov, and D. V. Minakov, J. Appl. Phys. **115**, 033506 (2014).

[10] G. I. Kanel', V. E. Fortov, and S. V. Razorenov, Phys.–Uspekhi **50**, 771 (2007).

[11] D. L. Preston, D. L. Tonks, and D. C. Wallace, J. Appl. Phys. **93**, 211 (2003).

[12] A. E. Mayer, K. V. Khishchenko, P. R. Levashov, and P. N. Mayer, J. Appl. Phys. **113**, 193508 (2013).

[13] B. J. Demaske, V. V. Zhakhovsky, N. A. Inogamov, and I. I. Oleynik, Phys. Rev. B **82**, 064113 (2010).

[14] B. J. Demaske, V. V. Zhakhovsky, N. A. Inogamov, and I. I. Oleynik, Phys. Rev. B **87**, 054109 (2013).

[15] D. B. Hayes, C. A. Hall, J. R. Asay, and M. D. Knudson, J. Appl. Phys. **96**, 5520 (2004).

[16] C. T. Seagle, J.-P. Davis, M. R. Martin, and H. L. Hanshaw, Appl. Phys. Lett. **102**, 244104 (2013).

[17] J. L. Ding, J. Mech. Phys. Solids **54**, 237 (2006).

[18] J. L. Ding and J. R. Asay, J. Appl. Phys. **101**, 073517 (2007).

[19] J. N. Johnson and L. M. Barker, J. Appl. Phys. **40**, 4321 (1969).

[20] J. W. Swegle and D. E. Grady, J. Appl. Phys. **58**, 692 (1985).

[21] G. I. Kanel, S. V. Razorenov, K. Baumung, and J. Singer, J. Appl. Phys. **90**, 136 (2001).

[22] Y. B. Zel'dovich and Y. P. Raizer, *Physics of Shock Waves and High-Temperature Hydrodynamic Phenomena* (Academic Press, New York, 1967).

[23] A. D. Sakharov, R. M. Zaidel', V. N. Mineev, and A. G. Oleinik, Sov. Phys.—Dokl. **91**, 1091 (1965).

[24] E. M. Bringa, K. Rosolankova, R. E. Rudd, B. A. Remington, J. S. Wark, M. Duchaineau, D. H. Kalantar, J. Hawreliak, and J. Belak, Nature Materials **5**, 805 (2006).

[25] D. K. Belashchenko, High Temp. **51**, 626 (2013).

[26] V. S. Krasnikov, A. E. Mayer, and A. P. Yalovets, Int. J. Plast. **27**, 1294 (2011).

[27] B. L. Rozhdestvensky and N. N. Yanenko, *Systems of Quasilinear Equations* (Nauka, Moscow, 1978).

[28] A. A. Charakhch'yan, Comp. Math. Math. Phys. **40**, 782 (2000).

[29] E. M. Vaziev, A. D. Gadzhiev, S. Y. Kuzmin, and A. V. Skovpen, AIP Conf. Proc. **849**, 465 (2006).

[30] I. P. Bazarov, *Thermodynamics* (MacMillan, New York, 1964).

[31] L. D. Landau and E. M. Lifshitz, *Fluid Mechanics* (Elsevier, Oxford, 1987).

[32] A. M. Kosevich, Sov. Phys.—Usp. **7**, 837 (1965).

[33] L. A. Merzhievsky and A. V. Tyagel'sky, J. de Physique **49**, 457 (1988).

[34] T. Suzuki, S. Takeuchi, and H. Yoshinaga, *Dislocation Dynamics and Plasticity* (Springer, Berlin, 1991).

[35] A. E. Dudorov and A. E. Mayer, Vestnik of the Chelyabinsk State University. Physics **12**, 48 (2011).

[36] J. von Neumann and R. D. Richtmyer, J. Appl. Phys. **21**, 232 (1950).

[37] K. V. Khishchenko, J. Phys.: Conf. Ser. **98**, 032023 (2008).

[38] L. D. Landau and E. M. Lifshitz, *Theory of Elasticity* (Elsevier, Oxford, 1986).

[39] M. W. Guinan and D. J. Steinberg, J. Phys. Chem. Solids **35**, 1501 (1974).

[40] J. Hirth and J. Lothe, *Theory of Dislocations* (Wiley, New York, 1982).

[41] V. A. Al'shitz and V. L. Indenbom, Sov. Phys.—Usp. **18**, 1 (1975).

[42] C. Kittel, *Introduction to Solid State Physics* (Wiley, New York, 2004).

[43] I. S. Grigoriev and E. Z. Meilikhov, eds., *Handbook of Physical Quantities* (CRC Press, Boca Raton, 1997).

[44] P. R. Levashov and K. V. Khishchenko, AIP Conf. Proc. **955**, 59 (2007).

[45] J. H. Hildebrand and R. H. Lamoreaux, Proc. Nat. Acad. Sci. **73**, 988 (1976).

[46] N. Jakse and A. Pasturel, Sci. Rep. **3**, 3135 (2013).

[47] D. Ceotto and F. Miani, High Temp. **51**, 568 (2013).

[48] V. N. Mineev and A. I. Funtikov, Phys.—Usp. **47**, 671 (2004).

[49] D. C. Swift, A. Seifter, D. B. Holtkamp, and D. A. Clark, Phys. Rev. B **76**, 054122 (2007).

[50] A. Seifter and D. C. Swift, Phys. Rev. B **77**, 134104 (2008).

TABLE I: Parameters of the model of elastoplastic properties: the shear modulus G_0 at normal conditions; the shear modulus derivatives G'_P and G'_T taken from Ref. 39; the portion of plastically dissipated energy α, which is spent on formation of new dislocations; the yield strength constant Y_0; the phonon drag parameter θ; the constant of interaction $A_{\rm I}$; the velocity of immobilization $V_{\rm I}$ and the minimal density ρ_0 taken from Ref. 12, where those were fitted to existing experimental profiles of free surface velocity at collision of metal plates; the annihilation constant k_a.

Metal	Al	Cu
G_0, GPa	23.3	47.7
G'_P	1.8	1.35
G'_T, GPa/kK	-17.2	-18
α	0.1	0.1
Y_0, MPa	22	30
θ, K	430	280
$A_{\rm I}$	6	4
$V_{\rm I}$, m/s	1.7	0.7
ρ_0, cm^{-2}	10^8	10^8
k_a	7	10

TABLE II: Slip systems in fcc metals.[40]

$n_x^\beta\sqrt{3}$	$n_y^\beta\sqrt{3}$	$n_z^\beta\sqrt{3}$	$b_x^\beta\sqrt{2}/b$	$b_y^\beta\sqrt{2}/b$	$b_z^\beta\sqrt{2}/b$
1	1	1	−1	0	1
			0	−1	1
			−1	1	0
−1	1	1	1	0	1
			0	−1	1
			1	1	0
1	−1	1	−1	0	1
			0	1	1
			1	1	0
−1	−1	1	1	0	1
			0	1	1
			−1	1	0

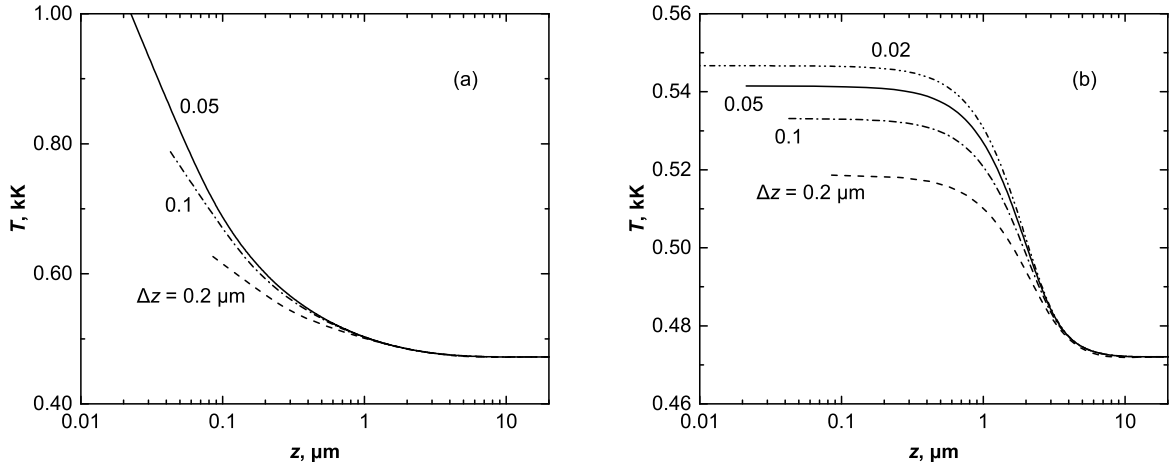

FIG. 1: High-entropy layer near the impact surface at symmetric collision of aluminum plates with velocity jump behind the shock wave $u = 1$ km/s at $t = 10$ ns, $\eta^* = 1$ Pa s: calculations with different mesh size Δz (a) without and (b) with taking into account the heat conductivity.

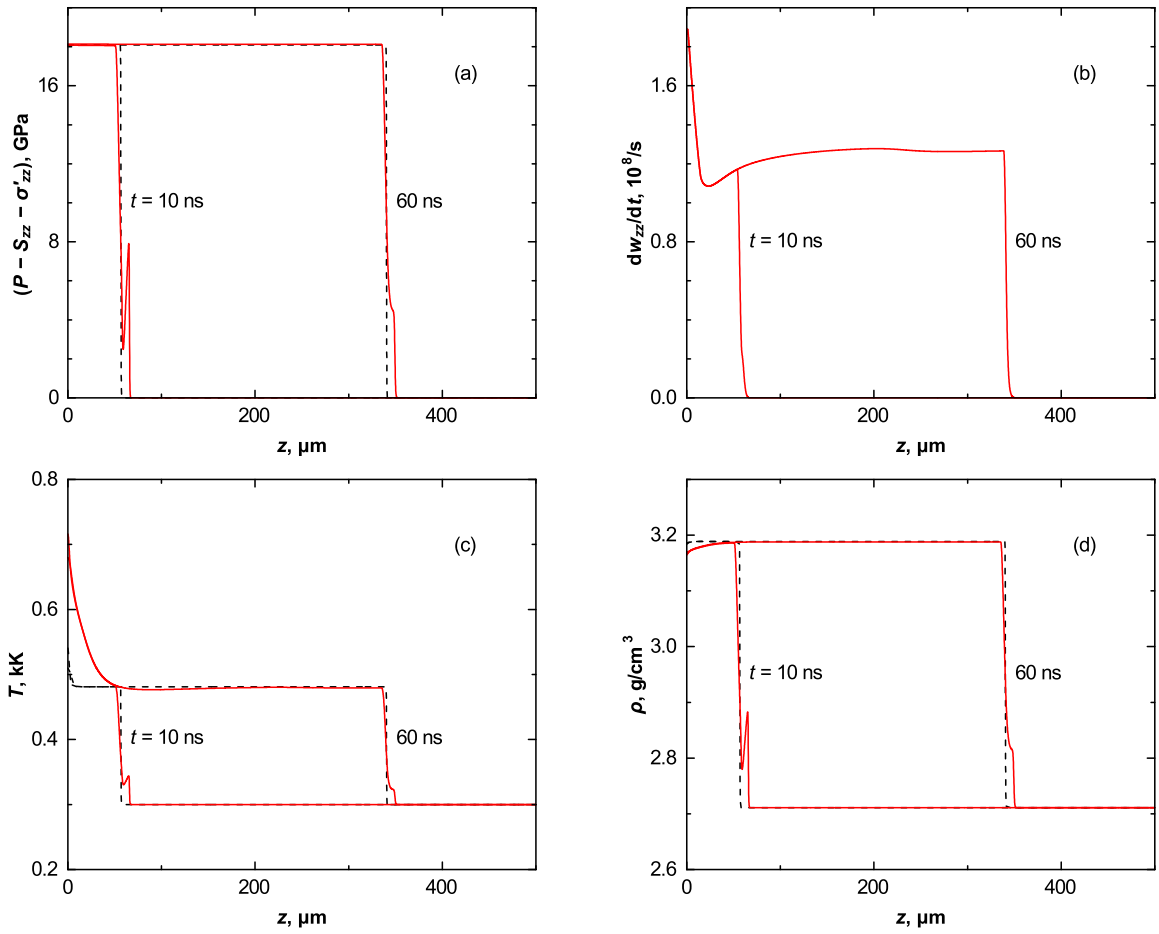

FIG. 2: Spatial distributions of (a) the longitudinal stress, (b) the maximal plastic strain rate, (c) the temperature and (d) the density at the symmetric collision of aluminum plates at $u = 1$ km/s: elastoplastic (a–d, solid line) and hydrodynamic (a, c, d, dash line) simulations. The maximal plastic strain rate (b) is taken as a maximum in each point of substance over all time starting from the beginning of impact.

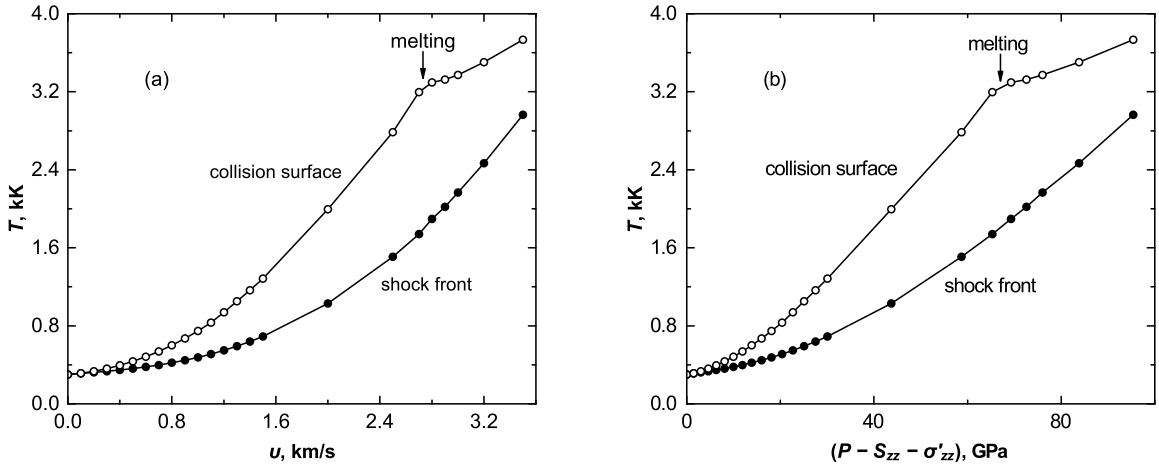

FIG. 3: Temperature on the collision surface in $t = 10$ ns after impact and behind the shock wave front versus (a) the particle velocity jump in the shock wave and (b) the longitudinal stress behind the shock wave. The arrows indicate the beginning of melting near the collision surface just after the instant of impact $t = 0$.

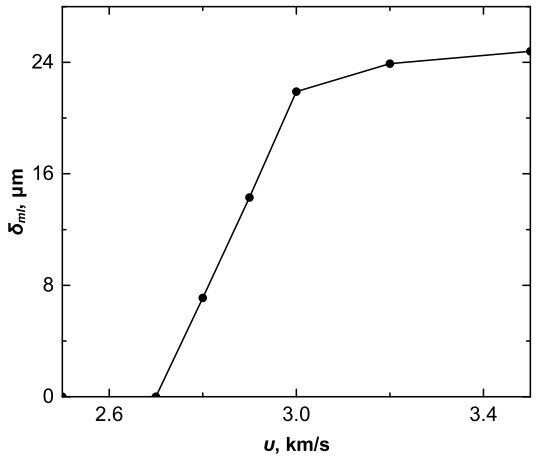

FIG. 4: Calculated thickness of molten layer near the impact surface (in the high-entropy layer) at collision of aluminum plates as a function of the particle velocity jump in the shock wave.

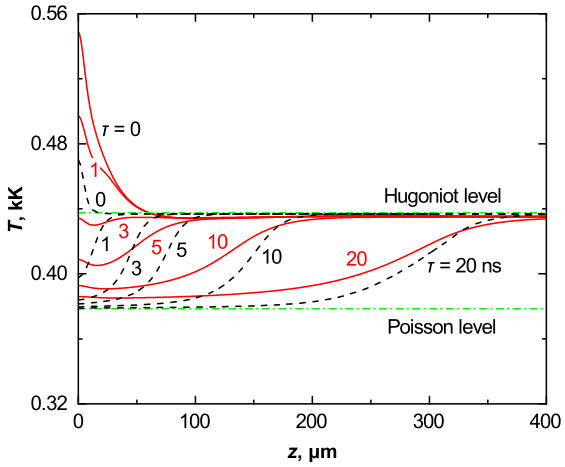

FIG. 5: Temperature profiles in non-isentropic layers near the loaded surface ($z = 0$) at ramp loading of aluminum with the maximal pressure $P_{\rm m} = 15$ GPa and various rise time $\tau = 0$, 1, 3, 5, 10 and 20 ns: elastoplastic (solid lines) and hydrodynamic (dash line) simulations.

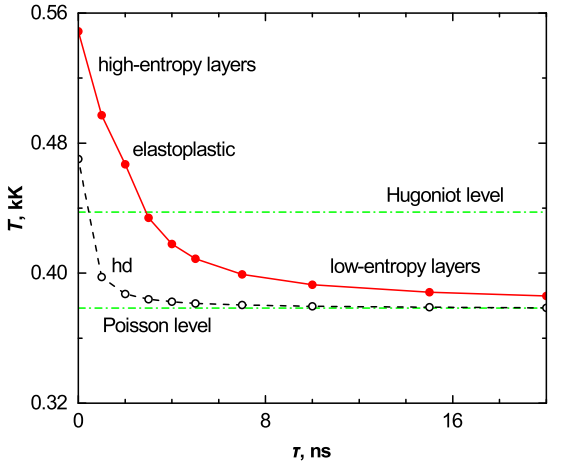

FIG. 6: The loaded surface temperature of aluminum at the loading pressure $P_{\rm m} = 15$ GPa as a function of the rise time: elastoplastic (solid line, solid circles) and hydrodynamic (dash line, open circles) simulations.

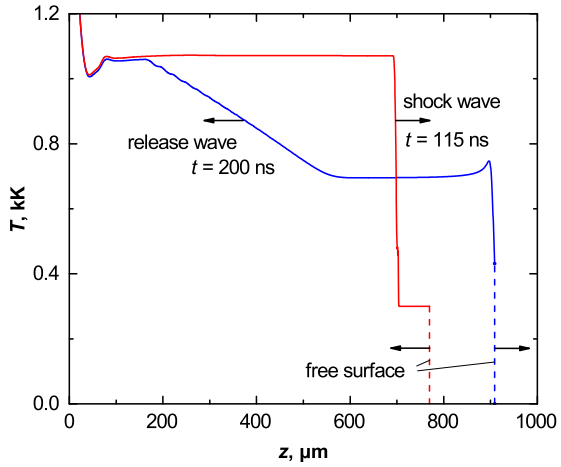

FIG. 7: Spatial distribution of the temperature in aluminum under the incident shock wave with $u = 2$ km/s and behind the release wave reflected from the sample free surface.

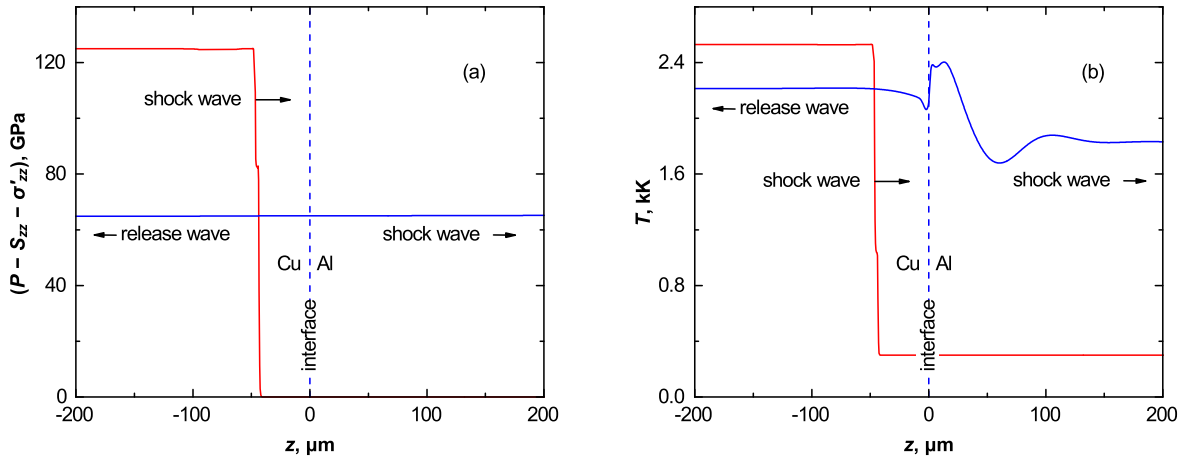

FIG. 8: Stress (a) and temperature (b) distribution near the interface (dashed line) between copper and aluminum before (red solid line) and after (blue solid line) the incidence of the shock wave with $u = 2$ km/s propogated from Cu to Al.

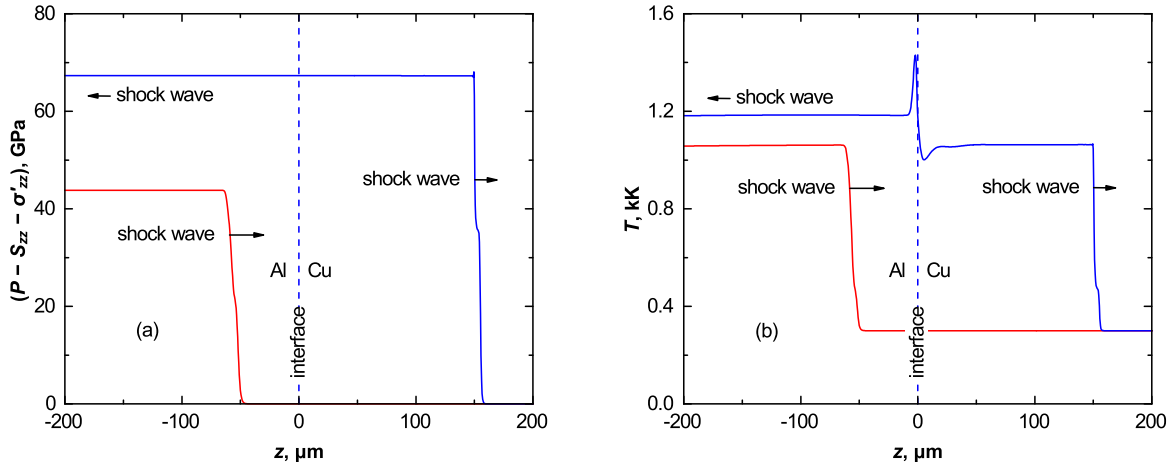

FIG. 9: Stress (a) and temperature (b) distribution near the interface (dashed line) between aluminum and copper before (red solid line) and after (blue solid line) the incidence of the shock wave with $u = 2$ km/s propogated from Al to Cu.